

Analysis of Preferred Mechanisms of CO Oxidation with Atomically Dispersed Pt₁/TiO₂ Using the Energetic Span Model

Selin Bac[†] and Shaama Mallikarjun Sharada^{*,†,‡}

[†]*Mork Family Department of Chemical Engineering and Materials Science, University of
Southern California, Los Angeles CA, USA 90089*

[‡]*Department of Chemistry, University of Southern California, Los Angeles CA, USA 90089*

E-mail: ssharada@usc.edu

Abstract

This work examines the mechanisms of low-temperature CO oxidation with atomically dispersed Pt on rutile TiO₂ (110) using density functional theory and the energetic span model (ESM). Of the 13 distinct pathways spanning Eley-Rideal (ER), termolecular ER (TER), Langmuir-Hinshelwood(LH), Mars-Van Krevelen (MvK) mechanisms as well as their combinations, TER with CO-assisted CO₂ desorption yields the highest turnover frequency (TOF). However, this pathway is ruled out because Pt is dynamically unstable in an intermediate state in the TER cycle, determined in a prior ab initio molecular dynamics study by our group. We instead find that a previously neglected pathway – the ER mechanism – is the most plausible CO oxidation route based on agreement with experimental TOFs and turnover-determining states. The preferred mechanism is sensitive to temperature, with LH becoming more favorable than ER and TER above 750 K. By comparing TOFs for Pt₁/TiO₂ with prior mechanistic

studies of various oxide-supported atomically dispersed catalysts in the literature, we also attempt to identify the most viable metal and support materials for CO oxidation.

Introduction

Atomically dispersed catalysts, consisting of precious metal atoms on oxide and other supports, constitute a promising way forward for sustainable heterogeneous catalysis as they have the potential to provide enhanced atom efficiencies for industrial and automobile applications.^{1–5} Also referred to as single atom catalysts, these materials combine the tunability associated with homogeneous catalysts consisting of transition metal complexes with ease of recovery of heterogeneous catalysts. Several experimental and computational studies have examined the surface chemistry and catalytic performance of these materials, most notably for CO oxidation,^{1,3,6–12} water gas shift (WGS),^{13–18} and CH₄ hydroxylation.^{19–21}

The principal challenges associated with the design of atomically dispersed catalysts include synthesis and stabilization of single atoms, enumeration and characterization of the metal coordination environment, and an understanding of dynamic response to the reactive environment.^{22–25} In the particular case of oxide-supported atomically dispersed catalysts, the metal atom can coordinate and interact with the support in several ways yielding active sites with distinct electronic properties that have a direct bearing on surface chemistry. Therefore, it is possible that reactions at these distinct binding sites might proceed via different mechanisms. This difficulty in determination of sites and site distributions, coupled with the likelihood of participation of metal clusters in catalysis,³ contributes to the wide range of observed activities as well as widely varying conclusions regarding catalyst viability and preferred mechanisms.⁶

Through scanning transmission electron microscopy (STEM) imaging and kinetics studies, Liu and coworkers demonstrate the formation of Pt clusters and nanoparticles under reaction conditions, which catalyze CO oxidation on Al₂O₃ and TiO₂ supports. Although

Pt single atoms can be stabilized on CeO_2 , clusters are more active than dispersed atoms in all three cases.³ On the other hand, DeRita and coworkers report the formation of stable isolated Pt sites on anatase TiO_2 , which exhibit two times higher turnover frequency (TOF) than 1 nm clusters.⁷ The authors propose a redox Mars-van Krevelen (MvK) mechanism, wherein the lattice oxygen participates in CO oxidation creating a surface vacancy over which O_2 dissociates. The MvK mechanism is proposed in experimental and computational studies of precious metals dispersed on reducible supports such as TiO_2 , CeO_2 , and FeO_x .^{1,23,26,27} The Langmuir-Hinshelwood (LH) mechanism, which involves chemisorption of all reacting species prior to activation, is typically preferred for precious metals supported on inert oxides such as in the case of $\text{Pt}_1/\text{Al}_2\text{O}_3$,²⁸ although this mechanism has also been examined computationally for Ru on both reducible and inert oxides including CeO_2 , TiO_2 , and Al_2O_3 .²⁹ The alternative Eley-Rideal (ER) mechanism, in which at least one species is in the gas phase and reacts directly with species adsorbed at the active site, is rarely examined on account of higher barriers.²⁹ However, a termolecular or tri-molecular ER mechanism has been proposed for CO oxidation over single atoms supported on two dimensional materials such as graphene,³⁰ bismuthene,³¹ and hexagonal boron nitride.³²⁻³⁴ This mechanism differs from the traditional ER as three distinct species react in a single step. In the case of CO oxidation, the ternary step occurs between two CO molecules co-adsorbed on the single atom and O_2 in the gas phase to simultaneously create two CO_2 molecules.

To develop a complete description of the activity of atomically dispersed catalysts, we need to examine not only the preferred mechanism – MvK, LH, ER, or a combination of these pathways – but also the sensitivity of these pathways to active site distributions. In addition, inferring preferred mechanisms or sites or even identifying the most active metal-support combination requires us to go beyond the conventional calculation of potential or free energy surfaces. This is because intuition alone cannot guide the identification of rate-limiting features in a multi-step pathway, and quantitative means to determine activity are necessary. The TOF of catalytic cycles is one such desired measure of site activity,³⁵ which

can be determined from quantum chemistry calculations of reaction pathways using the energetic span model (ESM). Developed by Shaik and coworkers, this model employs the fact that a TOF is dependent on the energetic span – the range of energies spanned by reaction intermediates and transition states in the elementary steps constituting a catalytic cycle at steady state.^{36–39}

While the most widely used practice for contrasting mechanisms or activities is to contrast barriers to the rate-limiting step in energy profiles,^{29–34} these can lead to erroneous conclusions. This is because the TOF is not always governed by the highest energy transition state and/or the lowest energy intermediate or even a single rate-limiting step.⁴⁰ Instead, ESM identifies two rate-limiting states that have the highest influence on TOF, known as the TOF-determining transition state (TDTS) and TOF-determining intermediate (TDI). The technique has found widespread applications in both homogeneous and heterogeneous catalysis including, more recently, single atom or atomically dispersed catalysis.⁴¹

In this work, our goal is to employ density functional theory (DFT) and the energetic span model to identify the most preferred mechanism for room-temperature CO oxidation with atomically dispersed Pt/TiO₂. For the strongest Pt-binding hollow site (H1) on pristine (vacancy-free) rutile TiO₂(110) as the representative site,^{25,42,43} we calculate free energy profiles and TOFs for Eley-Rideal (ER), Langmuir-Hinshelwood (LH), Mars van Krevelen (MvK) and combinations of these pathways. Pathways arising from CO co-adsorption and the formation of carbonate (CO₃) intermediates are also probed. Among 13 pathways examined in this study, the termolecular ER mechanism with CO co-adsorption yields the highest TOF. However, co-adsorption leads to a dynamically unstable active site. Comparison with experimental TOF, instead, indicates preference for an ER mechanism in which the first step consists of O₂ dissociation at the active site. Analysis of temperature-dependence of TOFs shows that the LH pathway is preferred at temperatures exceeding 750 K. Comparison of TOFs with prior mechanistic studies shows that metal doping (rather than adsorption) improves activity and Ru and Pd supported on FeOx and CeO₂ are more active towards CO

oxidation compared to Pt_1/TiO_2 .

Methods

The model construction and DFT procedure follows prior studies from our group that probe the dynamical evolution of Pt_1/TiO_2 .^{25,44} A 2×4 unit cell of the (110) surface of TiO_2 (12 Å vacuum) is employed to ensure that Pt atoms in repeating images are separated by at least 10 Å. Of the five layers used to construct the slab, only the top layer is relaxed in simulations while the remaining layers are frozen in their bulk positions. We employ the Atomic Simulation Environment (ASE) software⁴⁵ for model setup and the Vienna Ab Initio Simulation Package (VASP)^{46–49} for spin polarized DFT computations using the Strongly-Constrained and Appropriately-Normed (SCAN) meta-generalized gradient approximation (meta-GGA).⁵⁰ SCAN is chosen both here and in our prior studies as it has been shown to accurately predict not only bulk properties of binary oxides and correct relative stability of rutile and anatase phases,^{51–53} but also binding energies of adsorbates and water- TiO_2 surface dynamics.^{54,55} Section 1 of the Supporting Information (SI) provides further details of the methods employed in this study to compute CO oxidation pathways and free energies.

Unless stated otherwise, all free energy changes (ΔG) are calculated at 298 K. Intrinsic barriers are determined as the free energy difference between the transition state and the preceding initial state. We employ the TOF expression developed within the steady-state framework of ESM as means to identify the preferred mechanism of low-temperature CO oxidation over Pt_1/TiO_2 :^{37,38}

$$TOF = \frac{k_B T}{h} \frac{\exp(-\Delta G_r / RT) - 1}{\sum_{i,j=1}^N \exp(T_i - I_j - \delta G'_{i,j}) / RT} \quad (1)$$

where k_B and R are the Boltzmann and gas constants, respectively, h is the Planck's constant, and T is the temperature. T_i and I_j are the free energies of the i^{th} transition state and j^{th} intermediate, respectively, along an N -step catalytic cycle of reaction free energy ΔG_r . $\delta G'_{i,j}$

defines the ordering of the transition state with respect to the intermediate:^{37,38}

$$\delta G'_{i,j} = \begin{cases} \Delta G_r, & \text{if } i \geq j \\ 0, & \text{otherwise} \end{cases} \quad (2)$$

The turnover frequency determining intermediate (TDI) and transition state (TDTS) are identified as the states with the highest degree of TOF control, analogous to the concept of degree of rate control:⁵⁶

$$X_{TOF,T_i} = \frac{\sum_{j=1}^N \exp((T_i - I_j - \delta G'_{i,j})/RT)}{\sum_{i,j=1}^N \exp((T_i - I_j - \delta G'_{i,j})/RT)} \quad (3)$$

$$X_{TOF,I_j} = \frac{\sum_{i=1}^N \exp((T_i - I_j - \delta G'_{i,j})/RT)}{\sum_{i,j=1}^N \exp((T_i - I_j - \delta G'_{i,j})/RT)} \quad (4)$$

where X_{TOF,T_i} and X_{TOF,I_j} represent the degree of TOF control for i^{th} transition state and j^{th} intermediate, respectively. The sum of $X_{TOF,T_i}(X_{TOF,I_j})$ over all transition states (intermediates) is unity. The energetic span (δE) of the catalytic cycle is free energy difference between the TDTS and TDI, corrected by ΔG_r depending on the relative position of the two states.³⁷ TOFs and their temperature dependence are determined for 13 possible CO oxidation mechanisms. The highest TOFs obtained for Pt₁/TiO₂ are then contrasted with TOFs from proposed mechanisms and catalytic cycles in the literature for other oxide-supported atomically dispersed catalysts to identify the most active metal-support interface for CO oxidation.

Results

A single catalytic cycle for CO oxidation involves the formation of two CO₂ molecules, or $2\text{CO} + \text{O}_2 \rightarrow 2\text{CO}_2$. We examine the possibility that the mechanism of one half-cycle, or the formation of one CO₂ molecule, can be distinct from the other half cycle. Free energy

profiles are constructed for ER, TER, LH, and MvK pathways as well as their combinations by putting together two half-cycles. For ease of illustration, we separate the formation of the first and the second CO_2 , and present mechanistic results for the two half-cycles here. In this section, complete catalytic cycles are reported only for cases in which 2 CO molecules are simultaneously co-adsorbed at the Pt site. For the remaining possibilities, complete catalytic cycles are described in Section 2 (Figures S1-S11) of the SI.

First Half-Cycle

Eley-Rideal Mechanism

In an ER half-cycle, CO in the gas phase reacts with adsorbed oxygen (molecular or dissociated) at the Pt site. Figures 1 and 2 show two possible ER mechanisms for formation of the first CO_2 , with the latter including the formation of a carbonate (CO_3) intermediate. Figure 1 depicts molecular adsorption and subsequent dissociation of O_2 (black solid curve, $\text{i} \rightarrow \text{ii} \rightarrow \text{iii}$) as well as direct, dissociative adsorption (red dashed curve, $\text{i} \rightarrow \text{iii}$). Despite similar barriers to sequential adsorption and dissociation and direct dissociation, the two pathways yield distinct TOFs, described later in this section. Between (iii) and (iv), CO_2 is formed via the reaction of the dissociated O that is farther away from the support surface and a CO molecule in the gas phase. CO_2 formation and desorption occur simultaneously and this step is determined to be barrierless.

Figure 2 describes another possible ER half-cycle, where CO_3 is formed upon the (barrierless) reaction of CO with molecularly adsorbed O_2 . Unlike Figure 1, the alternative pathway that includes dissociated O_2 is not examined. This is because the direct formation of CO_3 may be less favorable owing to large separation between dissociated O species (3.318 Å). The formation of CO_3 is proposed in the literature for CO oxidation over Al_2O_3 , CeO_2 and MgO supported catalysts.^{28,57,58} This step ($\text{ii} \rightarrow \text{iii}$) is significantly downhill, and the resulting CO_3 intermediate is strongly bound to Pt. The first CO_2 is formed upon partial desorption of CO_3 , leaving behind a single adsorbed O on Pt. This formation and desorption ($\text{iii} \rightarrow \text{iv}$)

step has an intrinsic free energy barrier of 1.84 eV.

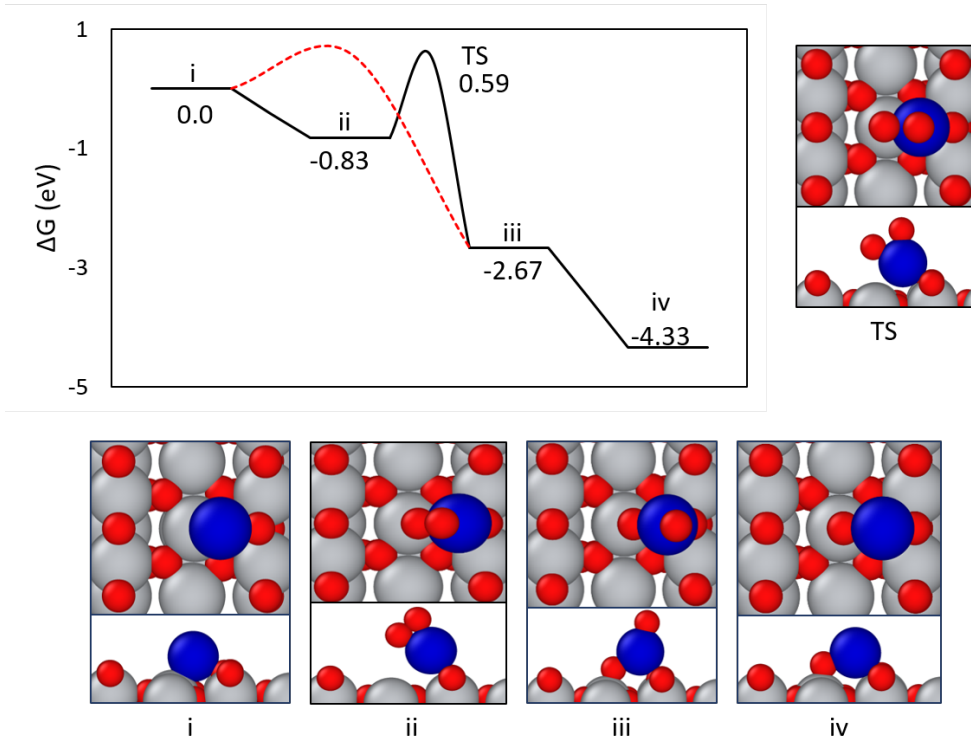


Figure 1: Free energy profile for the formation of the first CO_2 (first half-cycle) *via* the ER mechanism. The red dashed curve represents direct dissociative adsorption of O_2 . Top and side views of intermediates and transition states are also illustrated. (Color scheme – blue: Pt, red: O, grey: Ti, brown: C)

Langmuir-Hinshelwood Mechanism

Two possible LH routes are presented based on initial configurations consisting of Pt bound to O_2 and CO, shown in Figures 3 and 4, respectively. We do not examine the possibility of LH with dissociated O_2 because a stable structure with co-adsorbed CO and two O species cannot be found. In Figure 3, adsorption of CO (ii→iii) results in an increase in O–O separation from 1.353 Å (ii) to 1.440 Å (iii). The first CO_2 is formed between the co-adsorbed species with an intrinsic free energy barrier of 0.90 eV. Subsequent desorption of CO_2 is only slightly uphill in free energy.

Figure 4 describes the alternative LH pathway, where dissociative adsorption of O_2 follows CO adsorption. We note that although this is labeled as an LH pathway, dissociative O_2

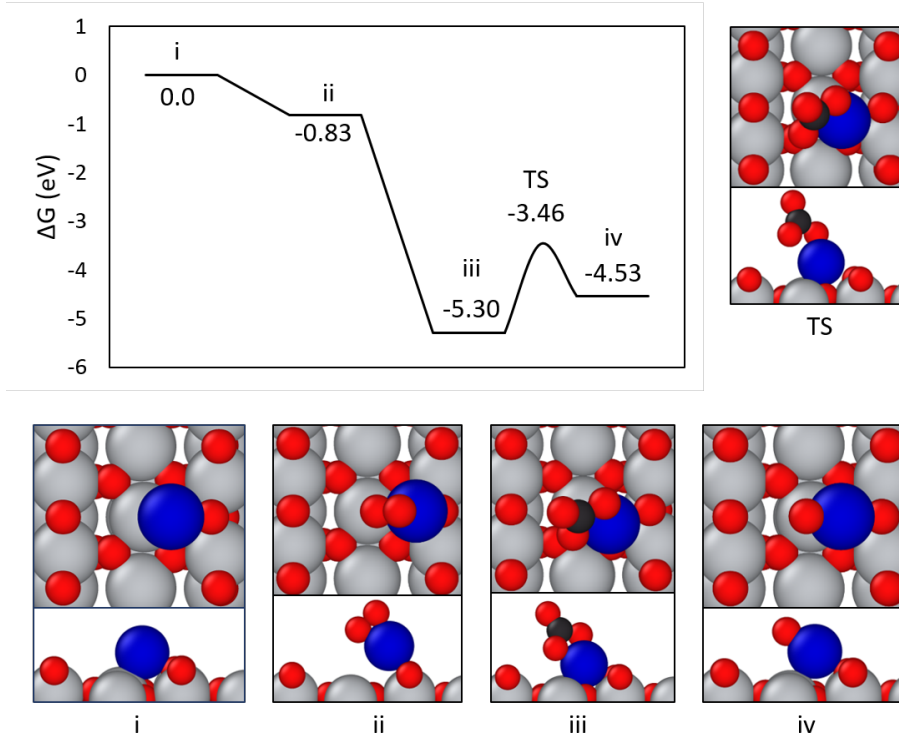


Figure 2: Free energy profile for the formation of the first CO_2 *via* the ER mechanism through a carbonate (CO_3) intermediate.

adsorption and CO_2 formation occur in a single step, blurring the distinction between LH and ER. CO_2 formation ($\text{ii} \rightarrow \text{iii}$) is followed by a barrierless reaction with adsorbed O to generate a CO_3 intermediate ($\text{iii} \rightarrow \text{iv}$). As CO_3 is a stable intermediate, subsequent formation and desorption of CO_2 are uphill in free energy.

The final states of the half cycles in Figures 1 and 3 are distinct from those in Figures 2 and 4. Shown in Figure 5, the free energies of the two geometries differ by 0.20 eV and are separated by a small barrier. The structure with O species that is less coordinated to the surface (ii) is lower in energy. The local site geometry consists of a near-linear O–Pt–O ($\angle \text{O-Pt-O} = 177.3^\circ$), reminiscent of thermally stable, linear oxide-like motifs identified in our previous *ab initio* molecular dynamics (AIMD) study of Pt binding configurations and dynamically stable O-bound Pt on rutile $\text{TiO}_2(110)$.^{25,44}

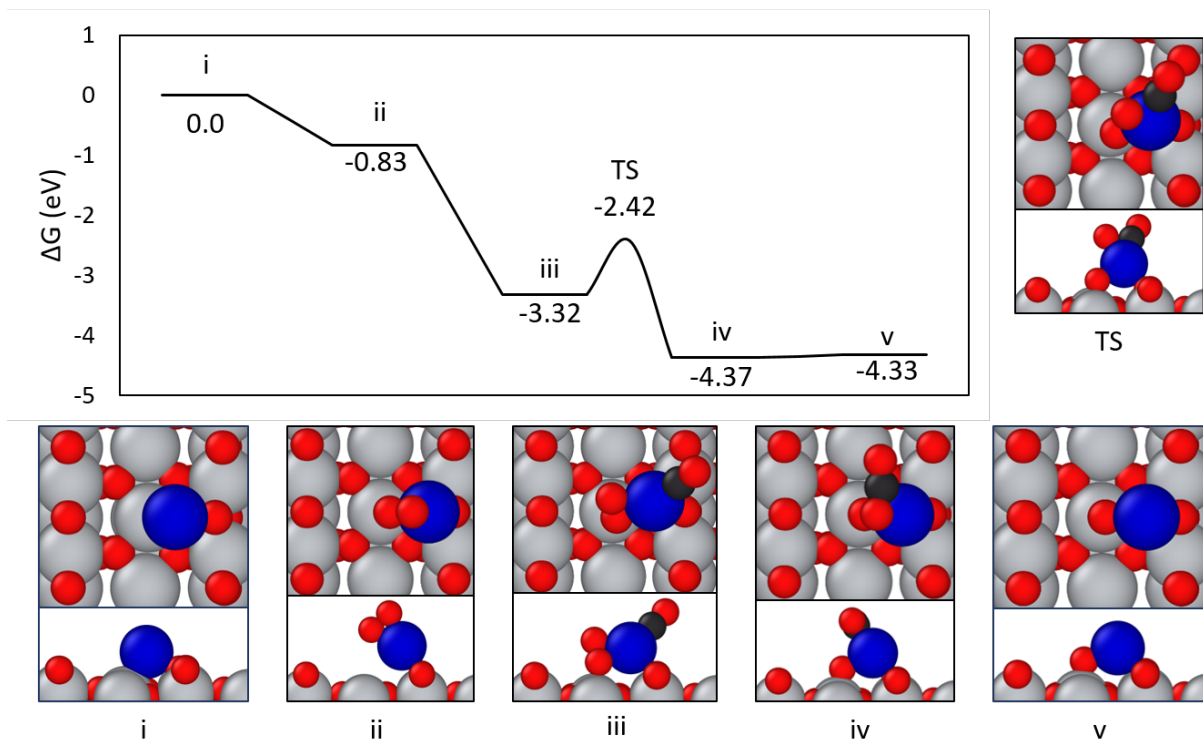


Figure 3: Free energy profile for the formation of the first CO_2 *via* the LH mechanism.

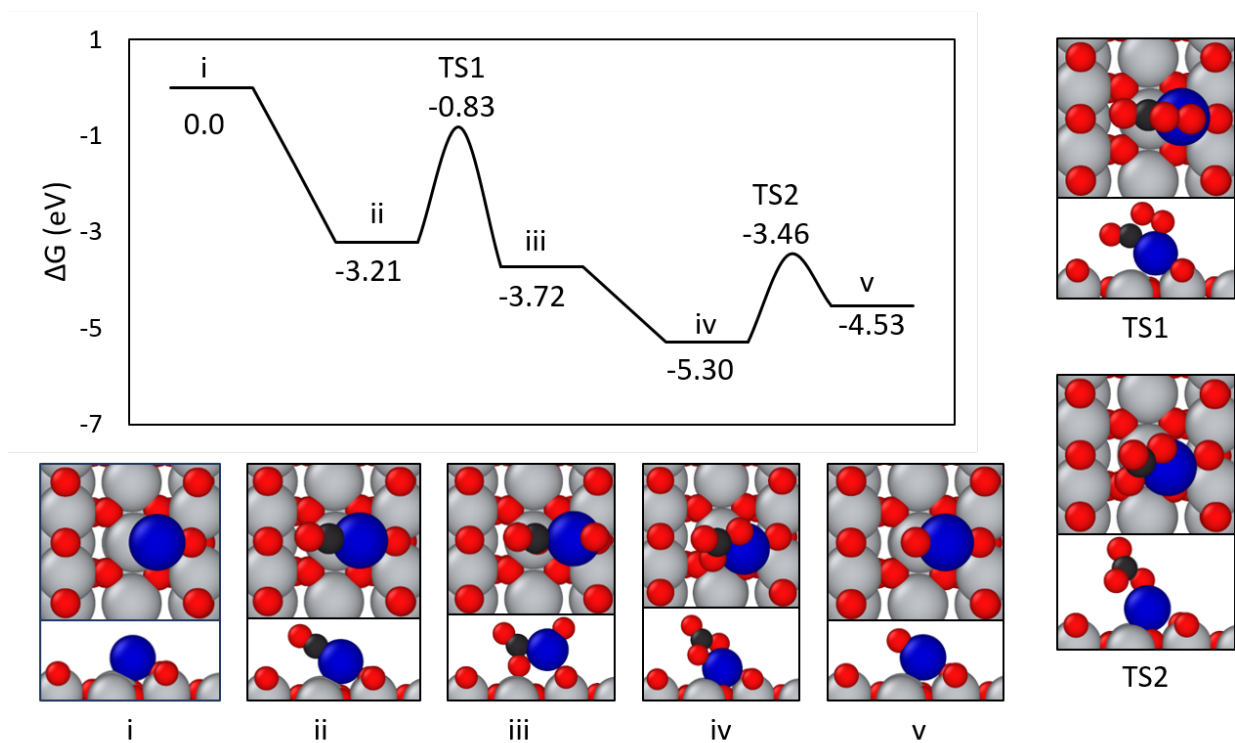


Figure 4: Free energy profile for the formation of the first CO_2 *via* the LH mechanism through carbonate intermediate (LH_{CO_3}).

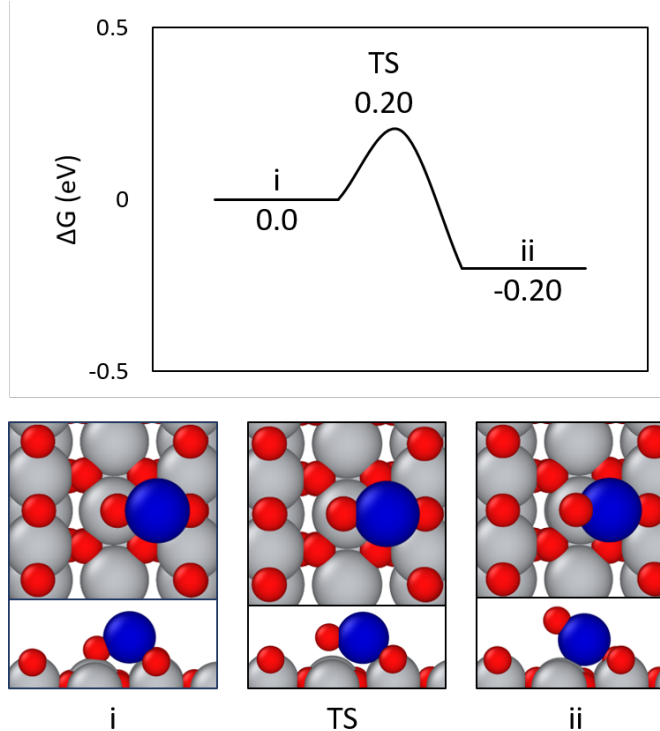


Figure 5: Diffusion of oxygen atom on Pt from more to less coordinated configuration.

Mars-van Krevelen Mechanism

In the MvK half-cycle (Figure 6), a TiO_2 lattice O reacts with an adsorbed CO, creating a vacancy upon CO_2 formation, which is then filled via O_2 adsorption and dissociation. O species at bridging positions are easier to remove compared to basal O.⁵⁹ Therefore the CO_2 formation step is preceded by migration of an adsorbed CO from the Pt site to the two-coordinated bridging O (O_{br}) atom (ii→iii(a)). The intrinsic free energy barrier associated with this step is very high (6.33 eV). An alternative possibility is the migration of lattice oxygen towards the adsorbed CO, represented in dashed red curves in Figure 6. This proceeds via a different transition state (TS1(b)), and the intrinsic free energy barrier is 0.94 eV lower than that of CO migration. The next step of CO_2 desorption proceeds via intrinsic free energy barriers of 2.03 eV and 2.58 eV relative to states iii(a) and iii(b) for CO and O migration pathways, respectively. The surface O vacancy is filled via barrierless adsorption and dissociation of O_2 (iv→v). One atom from the O_2 molecule fills the vacancy and the

other migrates towards the Pt, resulting in an O–O separation of 3.674 Å. The second half-cycle for MvK begins with state (v) and can proceed via ER or LH pathways. Since both possibilities yield identical rate determining states and TOFs, we report the results of only the pathway comprising MvK followed by ER.

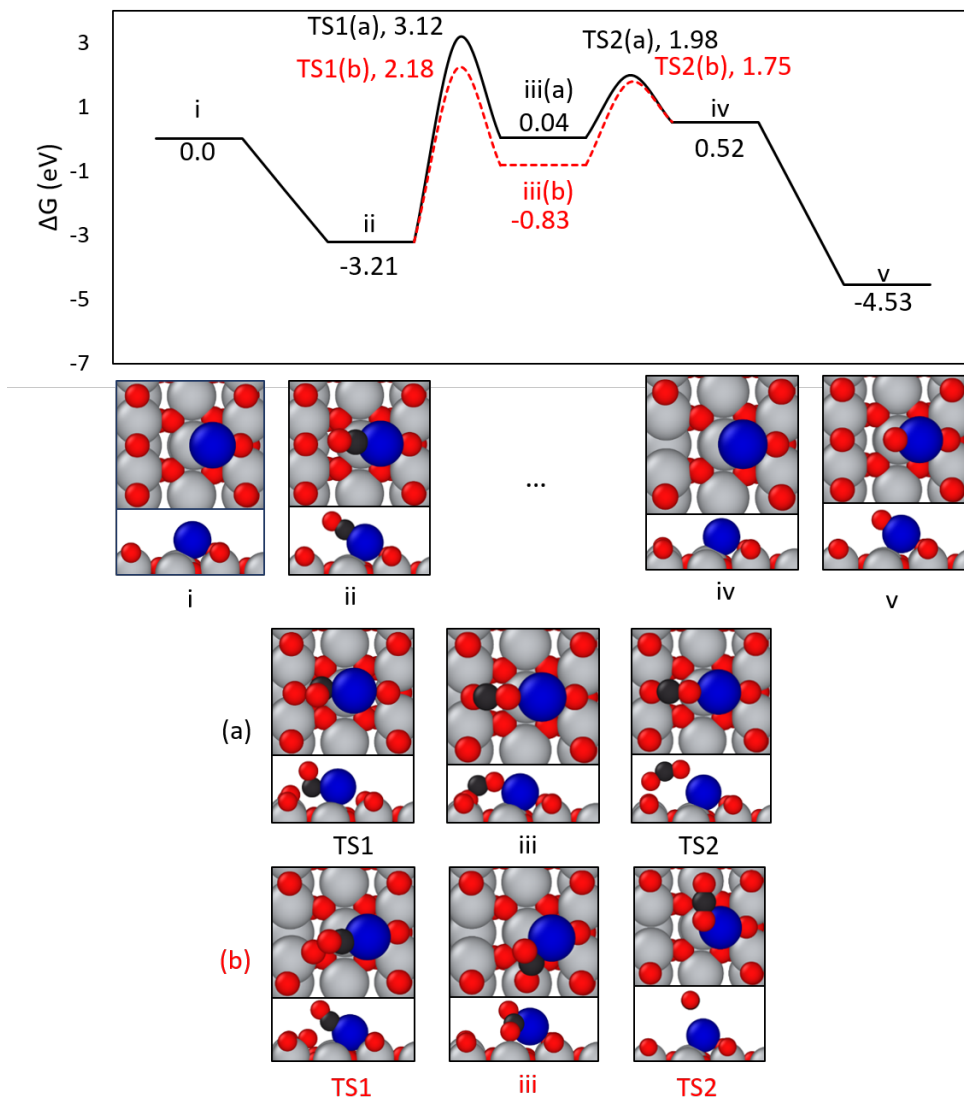


Figure 6: Free energy profile for the formation of the first CO₂ *via* the MvK mechanism, via either CO migration (black curve) or lattice oxygen migration (dashed red curve) steps between ii and iv.

Second Half-Cycle

Eley-Rideal Mechanism

Formation of the second CO_2 via the ER mechanism, shown in Figure 7, begins with an O-bound Pt site. This intermediate is obtained directly after the formation of the first CO_2 via ER (Figure 2), LH (Figure 4), or MvK (Figure 6). Alternatively, this intermediate can be obtained via O diffusion (Figure 5) after the ER or LH mechanisms described in Figures 1 and 3, respectively. CO in the gas phase reacts with O to form CO_2 , which is near-linear and coordinated weakly to Pt (Table S5, SI). Although the subsequent step of CO_2 desorption is uphill in free energy, a transition structure could not be identified, and therefore this desorption is treated as a barrierless step.

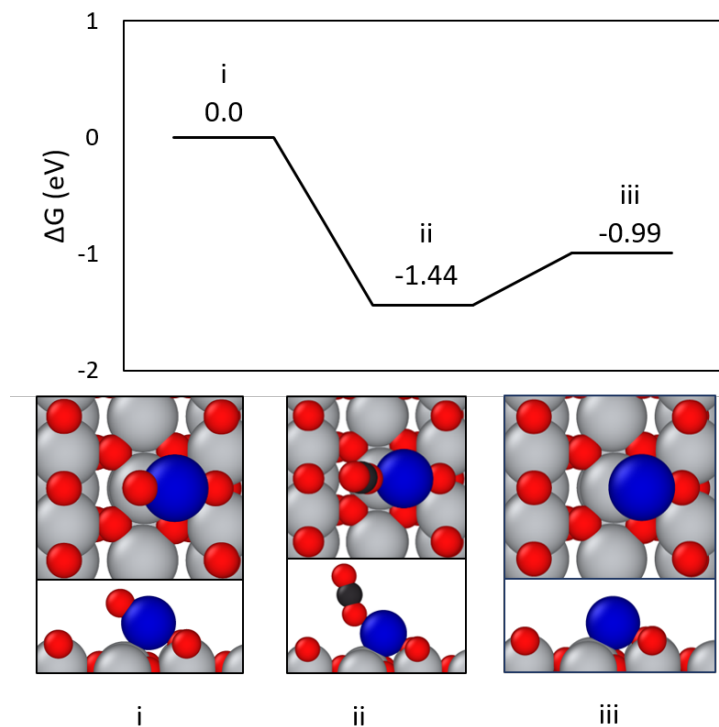


Figure 7: Free energy profile for the formation of the second CO_2 *via* the ER mechanism.

Langmuir-Hinshelwood Mechanism

Formation of the second CO_2 via the LH mechanism is depicted in Figure 8. After desorption of the first CO_2 in both ER or LH mechanisms (Figure 1 and 3, respectively), the O intermediate is coordinated to both Pt and adjacent five-coordinated Ti (Ti5c). The CO molecule binds to Pt, and reacts with O. This step (ii \rightarrow iii) proceeds via an intrinsic free energy barrier of 1.58 eV, and results in Pt-bound CO_2 that is bent ($\angle \text{O} - \text{C} - \text{O} = 138.8^\circ$). This bent structure is bound more strongly to the catalyst by 0.66 eV compared to the linear CO_2 shown in Figure 7. Desorption of this species is energetically uphill and proceeds via an intrinsic free energy barrier of 1.35 eV.

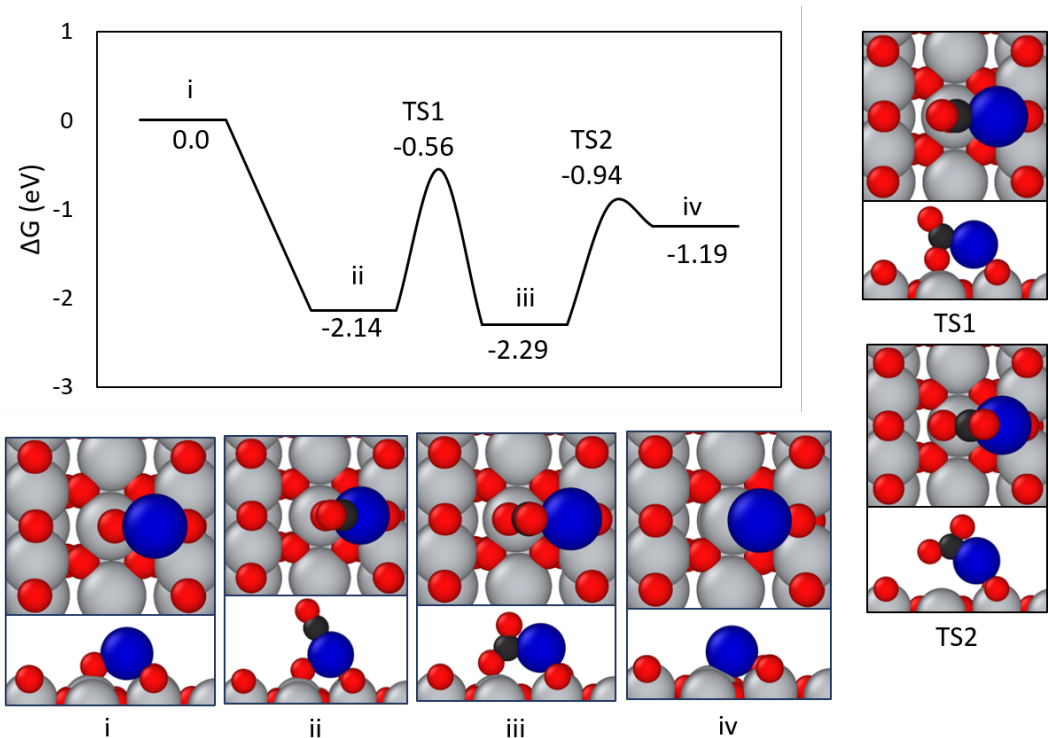


Figure 8: Free energy profile for the formation of the second CO_2 *via* the LH mechanism.

Co-Adsorption of Two CO Molecules

Prior mechanistic studies of the water-gas shift reaction initiate the catalytic cycle with a CO already bound to the active site with the underlying hypothesis that a strongly bound CO

is less likely to react but a second CO binds weaker to Pt and can therefore be oxidized.^{17,60} Here, we describe mechanisms and free energy profiles for when two COs are bound to Pt.

Termolecular Eley-Rideal Mechanism

Figure 9 portrays the full catalytic cycle of the termolecular ER mechanism involving the simultaneous formation of two CO₂ species (iii→iv). In this mechanism, two CO molecules co-adsorb on the Pt atom. The adsorption of the second CO is much weaker, associated with free energy lowering of only 0.12 eV compared to a single CO. The Pt–C distance of the first adsorbed CO increases by 0.02 Å when a second CO is adsorbed and this distance is 0.15 Å longer for the second adsorbate. Both CO molecules are activated with a single oxygen molecule at the same step. At the transition state, the O–O separation increases from 1.226 Å in gas phase to 1.271 Å and the intrinsic free energy barrier for this step is 0.87 eV. The less coordinated CO₂ desorbs with an intrinsic barrier of 0.74 eV. Desorption of the second, strongly coordinated CO₂ is less favorable, with an intrinsic barrier of 1.35 eV.

Co-Adsorption Assisted Termolecular Eley-Rideal Mechanism

Co-adsorption of more than one adsorbate at a metal site effectively weakens metal affinity towards each individual adsorbate, and therefore can facilitate desorption. For instance, the desorption of CO₂ may be aided by adsorption of a CO molecule. To analyze this scenario, we utilize a different reference state, corresponding to CO bound to Pt at the H1 site. Named **TER_{CO}**, the complete catalytic cycle for this pathway is shown in Figure 10. This pathway differs from the TER mechanism discussed previously only in the last step, in which a CO molecule is adsorbed prior to desorption of the second CO₂. This weakens CO₂ binding, thereby lowering the intrinsic barrier to CO₂ desorption to 0.96 eV.

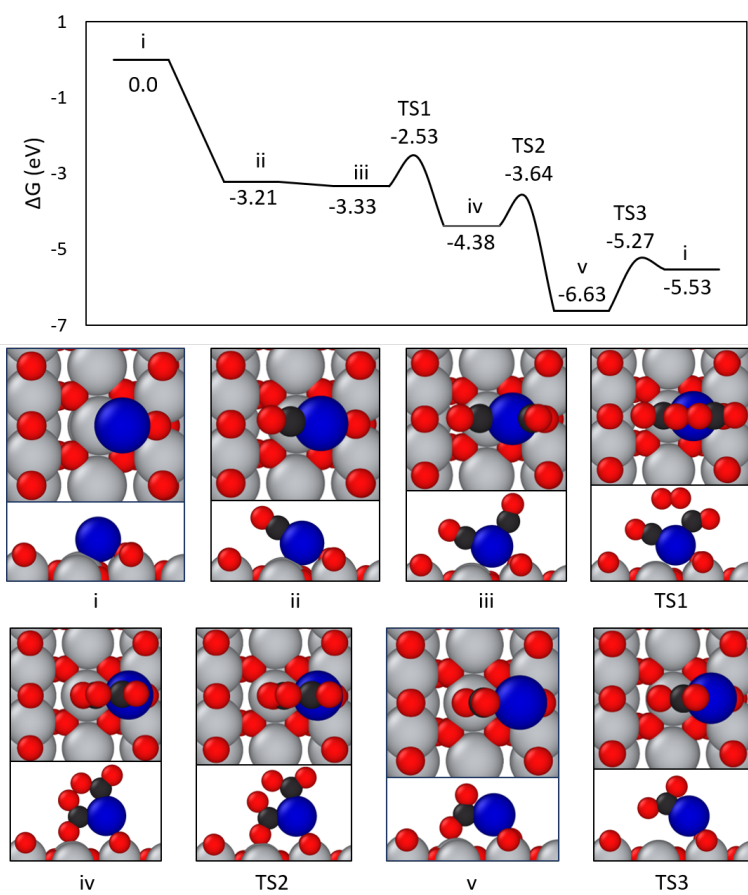


Figure 9: Free energy profile for the complete catalytic cycle with the TER mechanism.

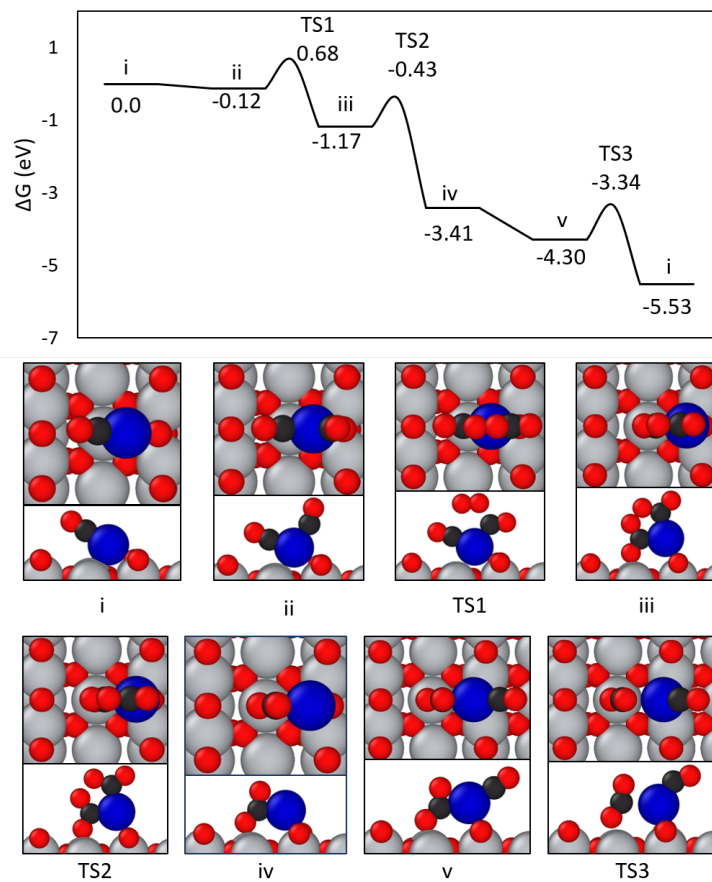


Figure 10: **TER_{CO}** – Free energy profile for the complete catalytic cycle with the TER mechanism, where the CO-bound Pt state serves as the reference.

Co-Adsorption Assisted Mars-van Krevelen Mechanism

The complete catalytic cycle for an alternative MvK mechanism beginning with co-adsorption of two CO molecules, labeled **MvK_{CO}**, is illustrated in Figure 11. The reference is identical to **TER_{CO}**. One of the CO molecules migrates towards the bridged O with an intrinsic free energy barrier of 3.47 eV, a little over half the barrier reported for CO migration in Figure 6. The subsequent intrinsic barrier to CO₂ desorption and vacancy formation is only 0.22 eV, significantly lower than that for the MvK pathway reported in Figure 6. Subsequent O₂ adsorption at the vacancy site proceeds with a small intrinsic barrier of 0.13 eV. O₂ adsorption is not fully dissociative and the O–O bond length increases from 1.226 Å in gas phase O₂ to 1.428 Å when bound to the vacancy (v). A barrier is not reported for this step as a first order saddle point could not be located using NEB. It is however reasonable to assume that this step is barrierless as complete dissociative adsorption at a vacancy site in the MvK cycle presented in Figure 6 (iv→v) is barrierless. In the mechanism presented in Figure 11, CO binding to Pt appears to suppress complete dissociation of O₂. The assumption that this step is barrierless does not affect the resulting TOF and subsequent comparison of mechanisms.

In step vi, another CO molecule binds to Pt. CO₂ is formed by the CO adsorbed closest to the O₂-bound vacancy site. Migration and CO oxidation occur in a single step, with an intrinsic barrier of 4.48 eV, which is higher than the barrier in the absence of an O₂-bound vacancy site (TS1 in Figure 11). An alternative pathway is possible from (v), shown in red dashed curves in Figure 11. This shows an ER mechanism, in which CO₂ is formed and desorbed upon reaction of vacancy-bound O with a CO molecule in the gas phase. This pathway (v→i) is energetically more favorable as it avoids the high barrier step associated with CO migration.

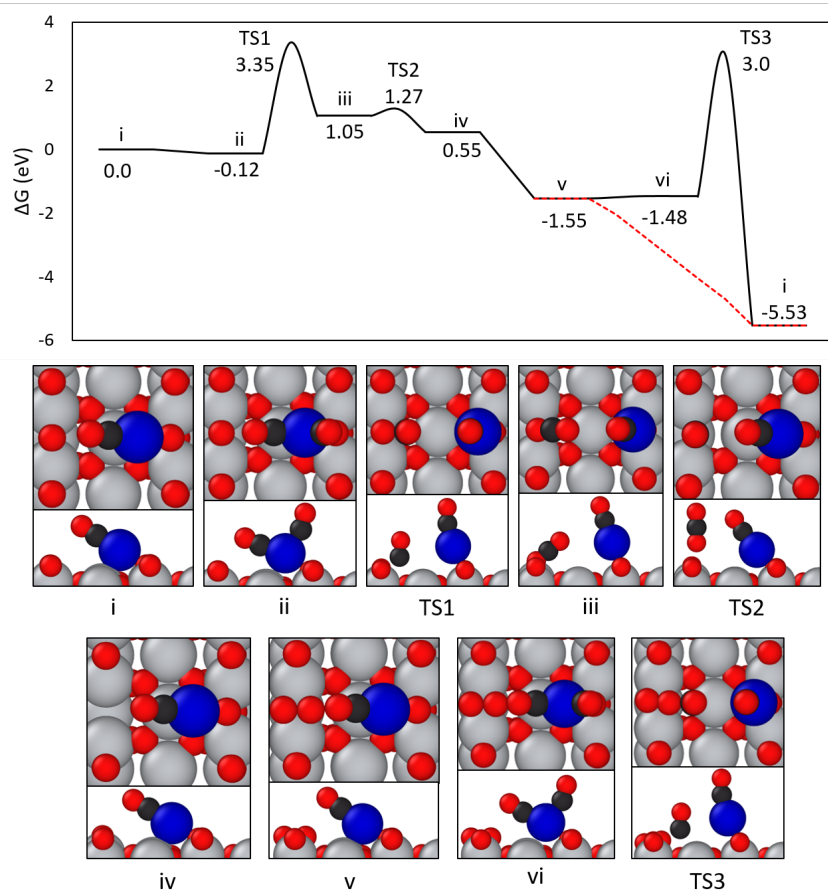


Figure 11: Free energy profile for the complete catalytic cycle with the MvK mechanism, where the CO-bound Pt state serves as the reference. The red dashed line represents a combination of MvK with the ER mechanism for formation of the second CO_2 .

Turnover Frequency Analysis: Energetic Span Model

We enumerate mechanistic possibilities for the full CO oxidation catalytic cycle by examining combinations of the first and second CO₂ formation mechanisms described above. Thirteen distinct pathways are identified and illustrated in Figures S1-S11 (Section 2, SI). TOF values of these cycles are reported in Table 1 along with the corresponding energetic spans, TDIs, and TDTSs. The naming convention for the pathways reported in Table 1 is as follows:

1. **ER (LH)**: catalytic cycle in which both CO₂ products are formed via ER (LH).
2. **ER_{CO3} (LH_{CO3})**: catalytic cycle involves the formation of a CO₃ intermediate.
3. **ER_{Odis}** and **ER_{Oads}**: ER pathways where O₂ is directly dissociated and dissociated after molecular adsorption, respectively, shown in Figure 1.
4. **ER+LH** and **LH_{CO3}+ER**: mixed mechanisms, with the name before and after the ‘+’ sign referring to the first and second halves of the catalytic cycle, respectively.
5. **TER**: termolecular ER, described in Figure 9.
6. **TER_{CO}** and **MvK_{CO}**: the pathways in which the reference state is the CO-bound Pt at the H1 site.
7. **MvK_{Omig}** and **MvK_{COmig}**: MvK pathways with lattice O and adsorbed CO migration, respectively, described in Figure 6.

The highest TOF for low-temperature CO oxidation with Pt₁/TiO₂ corresponds to **TER_{CO}** ($1.72h^{-1}$) followed by **ER_{Odis}** ($8.5 \times 10^{-2}h^{-1}$), while the lowest TOF corresponds to the **MvK_{COmig}** mechanism ($1.62 \times 10^{-91}h^{-1}$). Based on the ESM, the termolecular Eley-Rideal pathway with at least one CO adsorbed at the Pt site throughout the catalytic cycle is the most favorable route for room temperature CO oxidation over atomically dispersed Pt at H1 site of TiO₂ (110). The TDI and TDTS for this pathway are co-adsorbed CO and CO₂ (step v in Figure 10) and desorption of the second CO₂ (TS3 in Figure 10), respectively.

Excluding **TER_{CO}** and **ER_{O_{diss}}**, all pathways exhibit significantly lower TOFs spanning a wide range. For both ER and LH mechanisms, formation of the CO₃ intermediate decreases the TOF significantly, with the CO₃-bound state constituting a TDI for the former. All four MvK pathways examined in this study yield very low TOFs as they possess the largest energetic spans (δE , Table 1) compared to other mechanisms examined in this study.

ESM analysis shows that, with the exception of **ER_{O_{diss}}**, **ER+LH**, and **MvK_{CO}**, TDI and TDTS are successive states. In other words, if TDI and TDTS are successive states, the situation is equivalent to a ‘rate-limiting step’ in a multi-step pathway. This is illustrated in the δE and ΔG ($G_{TDTS} - G_{TDI}$) columns in Table 1. The two columns differ only for **ER_{O_{diss}}** and **ER+LH** because the TDTS appears before the TDI (Figures S2 and S3, SI). In most pathways reported in Table 1, TDI is the CO-bound state since CO adsorbs strongly to Pt at the H1 site. Although the TDTS in both **TER** and **TER_{CO}** is the desorption of the second CO₂, TOF of **TER_{CO}** is significantly higher since the desorption is aided by CO co-adsorption. Along similar lines, TOF values of MvK pathways with CO-bound references (**MvK_{CO}**, **MvK_{CO}+ER**) are significantly higher than those without CO co-adsorption (**MvK_{O_{mig}}**, **MvK_{CO_{mig}}**).

Table 1: TOF values and TOF-determining states (TDI and TDTS) of 13 low-temperature CO oxidation pathways over H1 site of Pt₁/TiO₂ catalyst. Points corresponding to TDI and TDTS along the reaction pathways are presented in Figures S1–S11 of the SI. The bottom three rows utilize CO-bound Pt at the H1 site as the reference for free energy calculations. Energetic span (δE) and difference between the free energies of TDTS and TDI ($\Delta G = G_{TDTS} - G_{TDI}$) are also presented.

Pathway	TOF (h^{-1})	TDI (Figure #, step #)	TDTS (TS#)	δE (eV)	ΔG (eV)
ER_{O_{diss}}	8.50×10^{-2}	linearly adsorbed CO ₂ (S1, vi)	dissociative O ₂ adsorption (TS1)	1.03	6.56
TER	2.51×10^{-7}	adsorbed bent CO ₂ (S7, v)	second CO ₂ desorption (TS3)	1.36	1.36
ER_{O_{ads}}	3.00×10^{-8}	adsorbed O ₂ (S1, ii)	O ₂ dissociation (TS1)	1.41	1.41
LH	3.98×10^{-11}	co-adsorbed CO and O (S4, vi)	second CO ₂ formation (TS2)	1.58	1.58
ER+LH	6.73×10^{-13}	adsorbed bent CO ₂ (S3, v)	dissociative O ₂ adsorption (TS1)	1.69	7.21
ER_{CO3}	2.27×10^{-15}	adsorbed CO ₃ (S2, iii)	first CO ₂ desorption (TS)	1.83	1.83
LH_{CO3}	1.09×10^{-24}	adsorbed CO (S5, ii)	first CO ₂ formation (TS1)	2.38	2.38
LH_{CO3}+ER	1.09×10^{-24}	adsorbed CO (S6, ii)	first CO ₂ formation (TS1)	2.38	2.38
MvK_{O_{mig}}	1.30×10^{-75}	adsorbed CO (S9, ii)	O migration (TS1)	5.39	5.39
MvK_{CO_{mig}}	1.62×10^{-91}	adsorbed CO (S8, ii)	CO migration (TS1)	6.33	6.33
TER_{CO}	1.72	co-adsorbed CO and CO ₂ (S10, v)	second CO ₂ desorption (TS3)	0.95	0.95
MvK_{CO}+ER	4.19×10^{-43}	co-adsorbed 2CO (S11, ii)	CO migration (TS1)	3.47	3.47
MvK_{CO}	2.48×10^{-61}	filled vacancy (S11, v)	second CO ₂ formation (TS3)	4.55	4.55

Temperature Dependence of TOF

The energetic span model employs free energies of intermediates and transition states constituting a catalytic cycle to compute TOFs. As these free energies vary with temperature and concentration, the sensitivity of proposed mechanisms to these quantities must be examined. Here, we examine only temperature dependence and neglect the effects of varying reactant and product partial pressures. The resulting temperature dependence of TOF across proposed mechanisms is shown in Figure 12. Owing to the wide range of TOF values observed, we employ a log-scale and reference TOF values to the highest TOF obtained at 298 K, corresponding to the **TER_{CO}** pathway. TOFs for the MvK mechanisms are not shown as these values are several orders of magnitude lower than the remaining pathways between 300 and 900 K. Figure 12 shows that each pathway exhibits distinct temperature sensitivity. While LH pathways (**LH**, **LH_{CO3}**, and **ER+LH**) result in higher TOF with increasing temperature, ER and **TER** pathways exhibit a maximum TOF in the range of temperatures examined, with **ER_{Oads}** and **ER_{Odiss}** mechanisms becoming indistinguishable after 720K. While **TER_{CO}** yields the highest TOF between 300 and 700 K, **TER** TOF is slightly higher than **TER_{CO}** between 700 and 750 K. Beyond about 750 K, **TER** TOF drops while TOFs of other pathways increase. At these elevated temperatures, **LH**, **ER_{CO3}**, **ER+LH**, and **ER** exhibit the highest TOFs.

Comparison with Prior Studies

We utilize ESM to calculate TOFs and contrast our mechanistic findings with prior computational studies of CO oxidation with atomically dispersed catalysts.^{1,9,10,26,27,29,58,61,62} Table 2 lists ESM results – TOF, TDI, TDTS – for previously proposed reaction mechanisms on oxide-supported atomically dispersed catalysts. As free energies are not always available in the literature, electronic energies are employed to calculate TOFs. The difference in the TOF value for the most preferred mechanisms in this study (**TER_{CO}**, **ER_{Odiss}**) between Tables 1 and 2 stems from the use of free and electronic energies, respectively. We note, however,

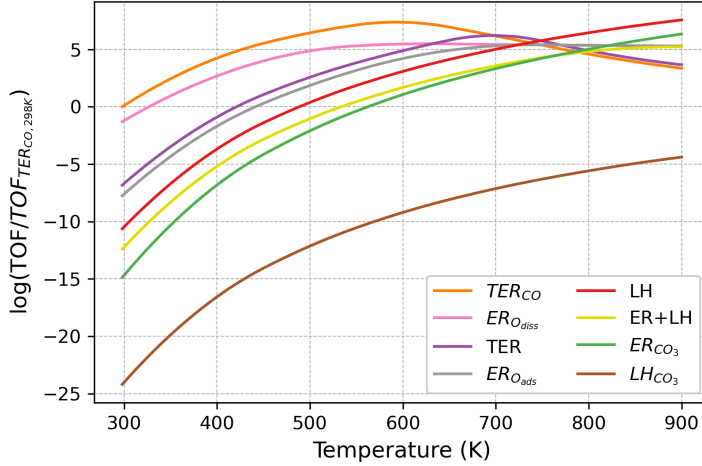


Figure 12: TOF evolution with temperature for select reaction mechanisms. Reference TOF is selected as **TER_{CO}** since it yields the highest TOF at 298 K (1.72 h^{-1}). MvK mechanisms are not included as their corresponding TOF values are significantly lower than others at these temperatures.

that the TOF values calculated using electronic and free energies are within an order of magnitude of each other at 298 K, as is to be expected. The mechanisms identified in prior studies are labeled MvK if a lattice oxygen leaves the surface in the oxidation product, and LH if all of the reactive species are adsorbed on the catalyst surface prior to the reaction step. We contrast the highest TOF in our study, obtained with the **TER_{CO}** mechanism, with TOF values calculated using DFT results from prior studies.

With the exception of Pt_1/MgO ⁵⁸ and Ir_1/FeO_x ,²⁶ all the systems reported in Table 2 have reaction pathways with successive TDI and TDTS. The TDI and TDTS are separated by a step in Pt_1/MgO and Ir_1/FeO_x , which implies that there is no single rate-limiting step in the preferred pathways for these systems. For MvK mechanisms reported in the literature, CO (or CO_2) adsorption and vacancy formation usually correspond to the TDI and TDTS, respectively. For the LH mechanisms, co-adsorbed intermediate states and CO_2 formation transition states typically constitute the TDI and TDTS, respectively. Co_1/FeO_x ²⁷ is the exception, reporting the formation of an OOCO-like structure between adsorbed CO and O_2 . This peroxo-type structure is distinct from CO_3 and is reported for CO oxidation with

Table 2: TOF analysis for CO oxidation at 298 K (unless noted otherwise) *via* proposed mechanisms in the literature with atomically dispersed metals supported(/) or doped(@) on metal oxides. TOF values reported in this table are calculated based on electronic energies (excluding zero point energies).

Catalyst	Mechanism	TOF (h^{-1})	TDI	TDTS
Pt ₁ /TiO ₂ (this work)	TER_{CO}	0.45	co-adsorbed CO and CO ₂	second CO ₂ desorption
Pt ₁ /TiO ₂ (this work)	ER_{O_{diss}}	0.10	linearly adsorbed CO ₂	dissociative O ₂ adsorption
Pt ₁ /FeO _x ¹	MvK	9.74×10^2	adsorbed CO ₂	vacancy formation
Pt ₁ /CeO ₂ ^{10,*}	MvK	8.94×10^{-6}	adsorbed CO	vacancy formation
Pt ₁ @CeO ₂ ⁶¹	MvK	1.15×10^8	filled vacancy	second CO ₂ formation
Pt ₁ /MgO ^{58,†}	LH	3.64	adsorbed CO	first CO ₂ formation
Ru ₁ /FeO _x ²⁷	LH	3.61×10^{11}	co-adsorbed CO and O	second CO ₂ formation
Ru ₁ /CeO ₂ ²⁹	LH	2.51×10^8	co-adsorbed CO and O	second CO ₂ formation
Pd ₁ /CeO ₂ ^{9,‡}	LH	1.68×10^{10}	adsorbed CO and 2O	second CO ₂ formation
Pd ₁ @ γ -Al ₂ O ₃ ⁶²	MvK	8.81×10^3	adsorbed CO ₂	vacancy formation
Rh ₁ /FeO _x ²⁷	MvK	2.31×10^7	adsorbed CO ₂	vacancy formation
Ir ₁ /FeO _x ²⁶	MvK	5.46×10^{-15}	adsorbed CO	vacancy formation
Co ₁ /FeO _x ²⁷	LH	5.48×10^8	co-adsorbed CO and O ₂	OOCO formation

* The calculation is based on zero-point corrected potential energies.

† The calculation is based on Gibbs free energies at 573 K.

‡ The calculation is based on Helmholtz free energies at 323 K.

the LH mechanism with Ru/CeO₂,²⁹ Cu₂O,⁶³ and Au-embedded graphene⁶⁴ catalysts. A stable peroxo-type structure is not detected with Pt₁/TiO₂ in our study.

Atomically dispersed Pt atoms supported or doped on various oxides yield TOF values ranging between 8.94×10^{-6} and 1.15×10^8 h⁻¹. The Pt₁/TiO₂ catalyst studied in this work yields higher TOF than Pt₁/CeO₂,¹⁰ although Pt doped on ceria⁶¹ leads to a TOF that is several orders of magnitude higher than Pt adsorbed on ceria or titania. Similarly, doped Pd on alumina (Pd₁@ γ -Al₂O₃) yields a large TOF via an MvK mechanism.⁶² The Pt₁/MgO study is carried out at 573 K, at which the TOF for Pt₁/TiO₂ is 7.93×10^6 and 4.39×10^2 h⁻¹ with **TER_{CO}** and **LH** mechanisms, respectively, both higher than Pt₁/MgO.⁵⁸ Similar to Pt, atomically dispersed Ru atoms exhibit higher activity when adsorbed on FeO_x rather than CeO₂. In both catalysts, the LH mechanism is preferred and the TDI and TDTS are identical. Higher activity of Ru₁/FeO_x²⁷ can be attributed to less favorable binding of CO₂.

Both MvK and LH mechanisms are proposed for atomically dispersed metals over FeO_x with TOF values ranging between 3.61×10^{11} for Ru₁/FeO_x²⁷ and 5.46×10^{-15} h⁻¹ for

Ir_1/FeO_x .²⁶ CO oxidation routes through LH mechanism have higher TOF values. Based on the ESM analysis of TOFs determined from the mechanisms proposed by these prior studies, we can rank the activities of single atoms adsorbed on FeO_x : $\text{Ru} > \text{Co} > \text{Rh} > \text{Pt} > \text{Ir}$. Similar to FeO_x , LH yields higher TOF values than MvK over CeO_2 catalysts, and metal activities decrease in the following order: $\text{Pd} > \text{Ru} > \text{Pt}$. Pt activity is higher when it is doped, and the MvK mechanism with $\text{Pt}_1@\text{CeO}_2$ ⁶¹ exhibits TOF comparable to LH over atomically dispersed Ru and Pd over ceria. The ESM-based TOF analysis can therefore be employed to contrast active sites across metal-support combinations and proposed mechanisms to identify the most viable species for CO oxidation.

Discussion

Significant experimental and computational efforts in the last decade have been aimed at uncovering the catalytic activity and underlying mechanisms of oxidation chemistry with atomically dispersed catalysts. While several studies implicitly assume an active role of the oxide support, or a Mars van Krevelen mechanism, we demonstrate here that there exist several mechanistic possibilities – combinations of MvK, LH, and ER as well as a range of intermediates and co-adsorption scenarios – which need to be evaluated to identify the pathway that yields the highest TOF. In a multi-step catalytic cycle, this cannot be accomplished solely by constructing a free energy profile and identifying the rate-limiting step or reaction bottleneck as the highest apparent barrier. This is because neither the highest energy point nor a single step in a catalytic cycle is necessarily the sole determinant of turnover frequency. The formation of a highly stable intermediate, for example, can inhibit the reaction and reduce TOF by poisoning the catalyst, as we see in the pathways that include CO_3 formation. Catalyst turnovers therefore must be determined by an ‘energetic span’ of intermediate and transition state energies, with a smaller span resulting in higher TOF.

We employ the energetic span model developed for the purpose of translating quantum

chemistry-based reaction energy profiles into catalyst TOFs. ESM reveals that there is no single rate-limiting step, or adjacent intermediate and transition state, in three pathways identified in this study – **ER_{Odiss}**, **ER+LH**, and **MvK_{CO}**. There can also be more than one intermediate or transition state that contributes to TOF. Using a degree of TOF control analysis (Equations 3 and 4), Table S1 (SI) reveals that **ER+LH**, **MvK_{CO}+ER**, and **MvK_{CO}** pathways have more than one intermediate that can control the TOF, although the degree of control by the TDI is significantly larger than any other intermediate. The ESM therefore emphasizes the importance of using quantitative methods for identifying rate- or turnover-determining states in a catalytic cycle, which will be critical to the determination of preferred mechanisms as well as catalyst tuning or design parameters.

We calculate TOFs for 13 possible pathways to identify the preferred mechanism of CO oxidation with atomically dispersed Pt at the hollow H1 site on the pristine (110) surface of TiO₂. The highest TOF at 298K corresponds to a modified ER pathway known as termolecular ER with CO co-adsorption (**TER_{CO}** in Table 1). In the absence of CO co-adsorption the termolecular pathway, **TER**, yields a TOF seven orders of magnitude smaller than that of **TER_{CO}**. Termolecular ER is proposed as the preferred mechanism of CO oxidation with single atoms supported on two-dimensional materials,⁶⁵ and is yet to be examined on oxide-supported catalysts. To the best of our knowledge, there is also no experimental evidence for the formation of a OCOOCO intermediate (step iv, iii in Figures 9 and 10, respectively).⁶ Co-adsorption, or the adsorption of more than one CO has been proposed in previous studies. For example, Ammal and Heyden propose a mechanism for the water-gas shift reaction based on one CO molecule being bound to CO throughout the catalytic cycle, in order to probe discrepancies in literature regarding the activities of single atoms vis-à-vis clusters.¹⁷ If co-adsorbed, CO consumption is not reflected in the disappearance of the infrared peak corresponding to Pt-bound CO, which was previously cited as evidence against single atoms (and in favor of clusters) being catalytically active by Ding and coworkers.⁶⁶ The study by Ammal and Heyden shows that co-adsorption leads

to weaker bound and more reactive species for WGS, which is also observed here for CO oxidation.

Despite evidence that co-adsorption leads to higher TOF, we need to take into account the fact that these conclusions are based on static quantum chemistry simulations where thermally driven motion of atoms is quenched. The role of finite temperature is partially accounted for by means of thermochemical approximations that enable the calculation of Gibbs free energies. Table S5 (SI) shows that the free energy of adsorption of two CO molecules is only marginally more favorable (0.12 eV downhill) relative to adsorption of a single CO at 298 K. Above 375 K, adsorption of a second CO molecule is no longer favorable. We also turn to dynamics studies to assess the viability of co-adsorption. In a recent study from our group, we utilize AIMD at 500 K to probe the evolution of adsorbate-bound Pt in the Pt₁/TiO₂ system over picosecond timescales.⁴⁴ While Pt exhibits very low mobility from its hollow, basal site when bound to a single CO in a 5 ps NVT trajectory at 500 K, we observe metal atom migration towards bridge sites even at room temperature upon co-adsorption, followed by complete separation of Pt(CO)₂ from the support before the system attains 500 K. Furthermore, the TER mechanism requires three species – two CO and one O₂ – to come together at the active site. The probability of these three species coming together, or the pre-exponential factor in the rate coefficient, is expected to be smaller for TER pathways compared to ER or LH. Therefore, despite yielding the largest TOF, our analysis of free energies and adsorbate-induced dynamics shows that the **TER_{CO}** pathway is less likely to be the preferred mechanism of CO oxidation.

Next, we consider the **ER_{O_{diss}}** pathway, which yields the second highest TOF of $8.50 \times 10^{-2} h^{-1}$ at 298 K. This is one of three ER pathways examined in this study – direct dissociative (**ER_{O_{diss}}**), molecular adsorption of O₂ followed by dissociation (**ER_{O_{ads}}**), and (**ER_{CO₃}**). Increasing temperature reduces the gap between **ER_{O_{diss}}** and **ER_{O_{ads}}** TOFs, leading to equal values at temperatures above 720 K, illustrated in Figure 12. As seen in Table 2, to the best of our knowledge, ER pathways have not been reported in prior computational studies

of CO oxidation with atomically dispersed catalysts. It can be argued that ER is a viable pathway particularly in cases where the barrier to formation of the TDTS – dissociative adsorption of O_2 – are low.^{9,26} We speculate that the competitive, favorable adsorption of CO and the possibility of CO_3 formation constitute reasons why the ER mechanism has not been proposed in previous studies.

We turn to experimental studies to determine the viability of ER mechanisms for CO oxidation. Direct experimental validation of the mechanism is challenging as the location and distribution of active sites are difficult to determine experimentally for comparison with site-averaged TOF computations. In addition, few direct comparisons are possible for the system under investigation in this work. Nevertheless, we contrast our results for the two most favorable pathways – **TER_{CO}** and **ER_{O_{diss}}** – with experimental TOFs for atomically dispersed Pt on TiO_2 reported by Liu and co-workers.³ Shown in Table S2 (SI) for temperatures between 373 and 448K, calculated TOFs ($0.033\text{--}3.75\text{ s}^{-1}$) for **ER_{O_{diss}}** are within an order of magnitude of experiment ($0.44\text{--}2.75\text{ s}^{-1}$), despite the rate of increase of TOF with temperature being higher in the former. On the other hand, the **TER_{CO}** pathway yields higher TOFs compared to experiment at all temperatures in this range, deviating by two orders of magnitude at 448 K. Furthermore, experimental studies with Pt dispersed on the anatase phase of TiO_2 find that O_2 dissociation is rate-limiting,^{7,23} in line with the TDTS identified by ESM for the **ER_{O_{diss}}** pathway. Although experiments propose O_2 dissociation as a rate-limiting step in the MvK mechanism, we find that all possible MvK pathways yield negligible TOFs. Therefore based on agreement with experiment in both TOF and TDTS and pending a complete derivation of the rate law, we believe that **ER_{O_{diss}}** is the preferred mechanism of CO oxidation for Pt dispersed on TiO_2 . It may be argued that the representative site chosen in this study is not the one that is most active towards CO oxidation in the experimental work by Liu and co-workers,³ particularly because Pt doping at cationic vacancies is expected to yield more active sites (Table 2). However, the experimental work reports Pt migration and the formation of clusters under CO oxidation conditions. This

observation is very much in line with AIMD work by our group described earlier in which Pt adsorbed (and not doped) at a basal site becomes highly mobile and dissociates from the surface when bound to more than one CO.⁴⁴ The dynamics of doped Pt at cationic vacancies are not reported by our group because Pt doping is significantly more energetically favorable than Pt adsorption, thereby introducing a steep barrier to metal atom migration and cluster formation.²⁵

While combined evidence from experiments, DFT, and AIMD points to **ER_Odiss** being the preferred pathway, we do not eliminate the possibility that the mechanism of CO oxidation may be site-sensitive or that more than one site may be involved in a single catalytic cycle. As reported in a previous study by our group, there are at least 17 distinct sites possible on the (110) surface, including cases where Pt occupies or is adjacent to cationic and anionic vacancies.²⁵ In addition to site-sensitivity, the dynamic adaptation of metal atoms to reaction conditions is difficult to account for in mechanistic studies.²³ Adsorbates have pronounced effect on metal-support interactions and can promote metal atom migration under reaction conditions. For instance, an AIMD study by our group finds that CO₂-bound Pt can diffuse easily towards the second hollow H2 site at 500 K, at which the adsorbate binding energy drops and CO₂ desorption becomes more favorable.⁴⁴ A similar phenomena is experimentally observed by Jakub and co-workers, where atomically dispersed Ir atoms on Fe₃O₄ migrate to a different adsorption site prior to desorption of CO from surface-bound Ir-dicarbonyl species.⁶⁷ Therefore, more than one metal binding site can participate in a single catalytic cycle. While we probe the preferred mechanisms at a single site in this study, the diversity in active sites as well as the dynamic character of single atoms requires an extensive analysis of *site-sensitivity* of mechanisms as well as the construction of *site-optimized* pathways that take into account diffusion between sites. To the best of our knowledge, these complexities are yet to be incorporated in mechanistic studies of atomically dispersed catalysts.

Despite low TOFs observed with the remaining 11 CO oxidation pathways, this study demonstrates the quantitative impact of co-adsorption, intermediates, and temperature on

TOFs. Co-adsorption of molecules aid the reaction by decreasing barriers to molecule migration or desorption. It is however important to consider the stability of these co-adsorbed structures under reaction conditions, as illustrated above in the case of **TER_{CO}**. The formation of a carbonate intermediate is significantly downhill in free energy, and the CO₃ intermediate is the TDI in **ER_{CO3}**. This is in line with prior studies which propose that CO₃ behaves as a catalyst poison.^{1,62,68}

The preferred mechanism of CO oxidation is sensitive to reaction temperature. Prior CO oxidation studies report temperature-sensitivity of preferred mechanisms with both supported nanoparticle and atomically dispersed catalysts.^{69,70} Figure 12 shows the shift in preference from **TER_{CO}** pathway at low temperatures to **LH** at temperatures above 750K. This is in part due to changes in kinetically relevant TDI and TDTS states with temperature.³ For example, at temperatures higher than 700 K, the TDI and TDTS of **TER** change to adsorbed CO and desorption of the first CO₂, respectively. TDI of the **TER_{CO}** becomes identical to that of the **TER** mechanism at temperatures above 600K. This causes a decrease in the TOF at higher temperatures. Similarly, the **TER** pathway exhibits a change in TDTS to desorption of the first CO₂ at temperatures above 700 K. ER pathways – **ER_{O_{ads}}** and **ER_{O_{diss}}**, exhibit an exponential increase in TOF followed by a plateau. The plateau coincides with the change of TDI of **ER_{O_{ads}}** and **ER_{O_{diss}}** mechanisms to the reference state (i in Figure 1) at temperatures above 700 K and 600 K, respectively. A change in rate-limiting state with temperature therefore is not necessarily indicative of a change in preferred mechanism. For the remaining mechanisms shown in Figure 12 (**LH**, **ER + LH**, **ER_{CO3}**, **LH_{CO3}**), TOFs increase monotonically and kinetically relevant states do not change with temperature.

This work utilizes ESM as means to discover both common features of and differences between catalytic cycles underlying various metal-support combinations identified for CO oxidation chemistry. Presented in Table 2, the most viable support for atomically dispersed Pt is CeO₂ and the active site is Pt doped at a cationic vacancy (Pt₁@CeO₂).⁶¹ This TOF is obtained by assuming an MvK pathway. While TDI’s vary across MvK pathways, the TDTS

for this catalyst, unlike others in Table 2, is not vacancy formation but rather the formation of the second CO_2 . Vacancy formation not being the TDTS is a possible consequence of the fact that the reverse spillover of a lattice oxygen to the metal atom is easier when the metal atom is doped and cationic.^{71–73} In general, low TOFs are associated with CO adsorption being the TDI (including Pt_1/TiO_2) and high TOFs are associated with CO_2 adsorption (or co-adsorbed CO and O) being the TDI. Owing to both high barrier to lattice O migration as well as strong CO binding,²⁶ the energetic span of the MvK mechanism is large for Pt_1/TiO_2 , leading to very small TOFs.

The analysis in Table 2 also highlights potential deficiencies in prior mechanistic studies and the ESM approach. An experimental study reports higher CO oxidation activity with Pt_1/FeO_x compared to Ir_1/FeO_x , and the TOF for the former is higher by one order of magnitude at 80 °C.²⁶ While the ESM analysis is in agreement with higher activity of Pt_1/FeO_x , the difference between calculated TOFs in Table 2 is significantly wider than experiment. It may be argued that the TOF analysis does not take into account concentration (or partial pressure) dependence of reaction mechanisms, whose contributions cannot be isolated from experimental turnovers.⁷⁴ However, similar to the prediction accuracies observed for Pt_1/TiO_2 reported in Table S2 (SI), the calculated TOF for Pt_1/FeO_x (0.27 s^{-1}) is very close to experiment (0.165 s^{-1}). On the other hand, calculated TOF for Ir_1/FeO_x catalysts is greatly underestimated. It is therefore more likely that the proposed reaction mechanism (MvK) is not the one that yields the highest TOF. The ESM-based TOF analysis therefore serves to identify incorrect mechanistic assignments in computational studies by means of validating calculated TOFs with experimentally observed trends.

It is important to note that an implicit assumption underlying the comparison of catalytic materials presented in Table 2 is that errors or uncertainties DFT-based potential energies used to compute TOFs are similar across all systems. The order of activities by support and metal atom proposed above therefore may be sensitive to the underlying choice of theory. These effects cannot be neglected because we find that a small increase in the energetic

span of, say TER_{CO} , by 0.02 eV doubles the TOF at 298 K. This sensitivity drops with increasing temperature, and the TOF increases by a factor of 1.5 with same increase in energy at 700 K. Therefore while our analysis of the 13 proposed pathways identifies the most viable mechanisms with a high level of confidence by using the same level of theory and thermochemical approximations, we will require further computations at similar if not identical levels of theory to identify the most active catalyst amongst those investigated in the literature with the same level of confidence.

Conclusions

Our understanding of the structure, operando behavior, activity, and stability of atomically dispersed catalysts is evolving rapidly. The energetic span model is a useful quantitative tool for characterizing catalytic activity as it offers direct means to not only contrast the viability of proposed mechanisms and validate with experiment, but also identify the most active catalyst for a desired reaction. This work combines ESM with an extensive study of CO oxidation mechanisms, AIMD studies of dynamical adsorbate effects, and experimental observations to show that MvK is not always the preferred mechanism on reducible oxide supports. Instead we find that a previously neglected possibility, the Eley-Rideal mechanism, is the most plausible mechanism even though it does not yield the highest TOF of all the pathways examined in this work. This finding is based on agreement of calculated TOFs with experiment as well as the TDTS with the experimentally proposed rate-limiting step. The highest TOF corresponds to a termolecular Eley-Rideal mechanism, which is ruled out mainly because Pt is dynamically unstable in an intermediate state in which two CO molecules are adsorbed at the active site. While the ER mechanism with dissociative adsorption of O_2 ($\text{ER}_{\text{O}_{\text{diss}}}$) is preferred at 298 K, the Langmuir-Hinshelwood mechanism becomes more favorable at temperatures higher than 750 K. We also use ESM to calculate TOF values and rate limiting states for several atomically dispersed catalysts reported in the literature

and attempt to identify the most active metal and support materials for CO oxidation. While the ESM provides a quantitative framework for comparing and validating proposed mechanisms, our examination of the preferred mechanism of CO oxidation is by no means complete. Owing to the diversity in site distributions achievable on these surfaces as well as the fact that the active sites themselves can change in the course of a catalytic cycle, future work in the field of atomically dispersed catalysts will involve the extensive examination of site-averaged and site-optimized kinetics.

Acknowledgement

Acknowledgment is made to the donors of The American Chemical Society Petroleum Research Fund (PRF 61149-DNI5). The authors are grateful to USC’s Center for Advanced Research Computing for computational infrastructure and support.

Supporting Information Available

Supporting Information contains the computational methods, complete catalytic cycles, results of Bader analysis, comparison with experimental data, and binding energy information of intermediates.

References

- (1) Qiao, B.; Wang, A.; Yang, X.; Allard, L. F.; Jiang, Z.; Cui, Y.; Liu, J.; Li, J.; Zhang, T. Single-atom catalysis of CO oxidation using Pt₁/FeO_x. *Nature Chemistry* **2011**, *3*, 634.
- (2) Flytzani-Stephanopoulos, M.; Gates, B. C. Atomically dispersed supported metal catalysts. *Annual review of Chemical and Biomolecular Engineering* **2012**, *3*, 545–574.
- (3) Liu, L.; Meira, D. M.; Arenal, R.; Concepcion, P.; Puga, A. V.; Corma, A. Determi-

- nation of the evolution of heterogeneous single metal atoms and nanoclusters under reaction conditions: which are the working catalytic sites? *ACS Catalysis* **2019**, *9*, 10626–10639.
- (4) Ding, S.; Hülsey, M. J.; Pérez-Ramírez, J.; Yan, N. Transforming energy with single-atom catalysts. *Joule* **2019**, *3*, 2897–2929.
 - (5) Li, X.; Yang, X.; Huang, Y.; Zhang, T.; Liu, B. Supported Noble-Metal Single Atoms for Heterogeneous Catalysis. *Advanced Materials* **2019**, *31*, 1902031.
 - (6) Zhang, H.; Fang, S.; Hu, Y. H. Recent advances in single-atom catalysts for CO oxidation. *Catalysis Reviews* **2020**, 1–42.
 - (7) DeRita, L.; Dai, S.; Lopez-Zepeda, K.; Pham, N.; Graham, G. W.; Pan, X.; Christopher, P. Catalyst architecture for stable single atom dispersion enables site-specific spectroscopic and reactivity measurements of CO adsorbed to Pt atoms, oxidized Pt clusters, and metallic Pt clusters on TiO₂. *Journal of the American Chemical Society* **2017**, *139*, 14150–14165.
 - (8) Qiao, B.; Liang, J.-X.; Wang, A.; Xu, C.-Q.; Li, J.; Zhang, T.; Liu, J. J. Ultrastable single-atom gold catalysts with strong covalent metal-support interaction (CMSI). *Nano Research* **2015**, *8*, 2913–2924.
 - (9) Spezzati, G.; Su, Y.; Hofmann, J. P.; Benavidez, A. D.; DeLaRiva, A. T.; McCabe, J.; Datye, A. K.; Hensen, E. J. Atomically dispersed Pd–O species on CeO₂(111) as highly active sites for low-temperature CO oxidation. *ACS Catalysis* **2017**, *7*, 6887–6891.
 - (10) Nie, L.; Mei, D.; Xiong, H.; Peng, B.; Ren, Z.; Hernandez, X. I. P.; DeLaRiva, A.; Wang, M.; Engelhard, M. H.; Kovarik, L., et al. Activation of surface lattice oxygen in single-atom Pt/CeO₂ for low-temperature CO oxidation. *Science* **2017**, *358*, 1419–1423.

- (11) Han, B.; Lang, R.; Tang, H.; Xu, J.; Gu, X.-K.; Qiao, B.; Liu, J. J. Superior activity of Rh₁/ZnO single-atom catalyst for CO oxidation. *Chinese Journal of Catalysis* **2019**, *40*, 1847–1853.
- (12) Hoang, S.; Guo, Y.; Binder, A. J.; Tang, W.; Wang, S.; Liu, J. J.; Huan, T. D.; Lu, X.; Wang, Y.; Ding, Y., et al. Activating low-temperature diesel oxidation by single-atom Pt on TiO₂ nanowire array. *Nature Communications* **2020**, *11*, 1–10.
- (13) Yang, M.; Allard, L. F.; Flytzani-Stephanopoulos, M. Atomically dispersed Au–(OH)_x species bound on titania catalyze the low-temperature water-gas shift reaction. *Journal of the American Chemical Society* **2013**, *135*, 3768–3771.
- (14) Lin, J.; Wang, A.; Qiao, B.; Liu, X.; Yang, X.; Wang, X.; Liang, J.; Li, J.; Liu, J.; Zhang, T. Remarkable performance of Ir₁/FeO_x single-atom catalyst in water gas shift reaction. *Journal of the American Chemical Society* **2013**, *135*, 15314–15317.
- (15) Gu, X.-K.; Huang, C.-Q.; Li, W.-X. First-principles study of single transition metal atoms on ZnO for the water gas shift reaction. *Catalysis Science & Technology* **2017**, *7*, 4294–4301.
- (16) Yang, M.; Liu, J.; Lee, S.; Zugic, B.; Huang, J.; Allard, L. F.; Flytzani-Stephanopoulos, M. A common single-site Pt(II)–O (OH)_x–species stabilized by sodium on “active” and “inert” supports catalyzes the water-gas shift reaction. *Journal of the American Chemical Society* **2015**, *137*, 3470–3473.
- (17) Ammal, S. C.; Heyden, A. Titania-Supported Single-Atom Platinum Catalyst for Water-Gas Shift Reaction. *Chemie Ingenieur Technik* **2017**, *89*, 1343–1349.
- (18) Zhu, S.; Wang, H.; Wan, K.; Guo, L.-J.; He, T.; Shi, X. Water–Gas Shift Reaction on Titania-Supported Single-Metal-Atom Catalysts: The Role of Cation (Ti) and Oxygen Vacancy. *The Journal of Physical Chemistry C* **2021**,

- (19) Tang, W.; Hu, Z.; Wang, M.; Stucky, G. D.; Metiu, H.; McFarland, E. W. Methane complete and partial oxidation catalyzed by Pt-doped CeO₂. *Journal of Catalysis* **2010**, *273*, 125–137.
- (20) Kwon, Y.; Kim, T. Y.; Kwon, G.; Yi, J.; Lee, H. Selective activation of methane on single-atom catalyst of rhodium dispersed on zirconia for direct conversion. *Journal of the American Chemical Society* **2017**, *139*, 17694–17699.
- (21) Shan, J.; Li, M.; Allard, L. F.; Lee, S.; Flytzani-Stephanopoulos, M. Mild oxidation of methane to methanol or acetic acid on supported isolated rhodium catalysts. *Nature* **2017**, *551*, 605–608.
- (22) Li, H.; Wang, M.; Luo, L.; Zeng, J. Static Regulation and Dynamic Evolution of Single-Atom Catalysts in Thermal Catalytic Reactions. *Advanced Science* **2019**, *6*, 1801471.
- (23) DeRita, L.; Resasco, J.; Dai, S.; Boubnov, A.; Thang, H. V.; Hoffman, A. S.; Ro, I.; Graham, G. W.; Bare, S. R.; Pacchioni, G., et al. Structural evolution of atomically dispersed Pt catalysts dictates reactivity. *Nature Materials* **2019**, *18*, 746–751.
- (24) Tang, Y.; Asokan, C.; Xu, M.; Graham, G. W.; Pan, X.; Christopher, P.; Li, J.; Sautet, P. Rh single atoms on TiO₂ dynamically respond to reaction conditions by adapting their site. *Nature Communications* **2019**, *10*, 1–10.
- (25) Humphrey, N.; Bac, S.; Mallikarjun Sharada, S. Ab Initio Molecular Dynamics Reveals New Metal-Binding Sites in Atomically Dispersed Pt₁/TiO₂ Catalysts. *The Journal of Physical Chemistry C* **2020**, *124*, 24187–24195.
- (26) Liang, J.-X.; Lin, J.; Yang, X.-F.; Wang, A.-Q.; Qiao, B.-T.; Liu, J.; Zhang, T.; Li, J. Theoretical and Experimental Investigations on Single-Atom Catalysis: Ir₁/FeO_x for CO Oxidation. *The Journal of Physical Chemistry C* **2014**, *118*, 21945–21951.

- (27) Li, F.; Li, Y.; Zeng, X. C.; Chen, Z. Exploration of high-performance single-atom catalysts on support M_1/FeOx for CO oxidation via computational study. *ACS Catalysis* **2015**, *5*, 544–552.
- (28) Moses-DeBusk, M.; Yoon, M.; Allard, L. F.; Mullins, D. R.; Wu, Z.; Yang, X.; Veith, G.; Stocks, G. M.; Narula, C. K. CO oxidation on supported single Pt atoms: experimental and ab initio density functional studies of CO interaction with Pt atom on $\theta\text{-Al}_2\text{O}_3$ (010) surface. *Journal of the American Chemical Society* **2013**, *135*, 12634–12645.
- (29) Li, F.; Li, L.; Liu, X.; Zeng, X. C.; Chen, Z. High-performance Ru1/CeO_2 single-atom catalyst for CO oxidation: a computational exploration. *ChemPhysChem* **2016**, *17*, 3170–3175.
- (30) Xu, G.; Wang, R.; Yang, F.; Ma, D.; Yang, Z.; Lu, Z. CO oxidation on single Pd atom embedded defect-graphene via a new termolecular Eley-Rideal mechanism. *Carbon* **2017**, *118*, 35–42.
- (31) Pan, W.; Zhao, B.; Qi, N.; Chen, Z. Pt-embedded bismuthene as a promising single-atom catalyst for CO oxidation: A first-principles investigation. *Molecular Catalysis* **2021**, *501*, 111379.
- (32) Mao, K.; Li, L.; Zhang, W.; Pei, Y.; Zeng, X. C.; Wu, X.; Yang, J. A theoretical study of single-atom catalysis of CO oxidation using Au embedded 2D h-BN monolayer: a CO-promoted O_2 activation. *Scientific Reports* **2014**, *4*, 1–7.
- (33) Lu, Z.; Lv, P.; Xue, J.; Wang, H.; Wang, Y.; Huang, Y.; He, C.; Ma, D.; Yang, Z. Pd 1/BN as a promising single atom catalyst of CO oxidation: a dispersion-corrected density functional theory study. *RSC Advances* **2015**, *5*, 84381–84388.
- (34) Lu, Z.; Lv, P.; Liang, Y.; Ma, D.; Zhang, Y.; Zhang, W.; Yang, X.; Yang, Z. CO oxidation catalyzed by the single Co atom embedded hexagonal boron nitride nanosheet: a DFT-D study. *Physical Chemistry Chemical Physics* **2016**, *18*, 21865–21870.

- (35) Kozuch, S.; Martin, J. M. L. “Turning Over” Definitions in Catalytic Cycles. *ACS Catalysis* **2012**, *2*, 2787–2794.
- (36) Kozuch, S.; Shaik, S. A combined kinetic-quantum mechanical model for assessment of catalytic cycles: Application to cross-coupling and Heck reactions. *Journal of the American Chemical Society* **2006**, *128*, 3355–3365.
- (37) Kozuch, S.; Shaik, S. Kinetic-quantum chemical model for catalytic cycles: the Haber-Bosch process and the effect of reagent concentration. *The Journal of Physical Chemistry A* **2008**, *112*, 6032–6041.
- (38) Kozuch, S.; Shaik, S. How to conceptualize catalytic cycles? The energetic span model. *Accounts of Chemical Research* **2011**, *44*, 101–110.
- (39) Uhe, A.; Kozuch, S.; Shaik, S. Automatic analysis of computed catalytic cycles. *Journal of Computational Chemistry* **2011**, *32*, 978–985.
- (40) Kozuch, S.; Martin, J. M. The Rate-Determining Step is Dead. Long Live the Rate-Determining State! *ChemPhysChem* **2011**, *12*, 1413–1418.
- (41) Falivene, L.; Kozlov, S. M.; Cavallo, L. Constructing bridges between computational tools in heterogeneous and homogeneous catalysis. *ACS Catalysis* **2018**, *8*, 5637–5656.
- (42) Iddir, H.; Ögüt, S.; Browning, N. D.; Disko, M. M. Adsorption and diffusion of Pt and Au on the stoichiometric and reduced TiO₂ rutile (110) surfaces. *Physical Review B* **2005**, *72*, 081407.
- (43) Chang, T.-Y.; Tanaka, Y.; Ishikawa, R.; Toyoura, K.; Matsunaga, K.; Ikuhara, Y.; Shibata, N. Direct imaging of Pt single atoms adsorbed on TiO₂ (110) surfaces. *Nano Letters* **2013**, *14*, 134–138.
- (44) Humphrey, N.; Bac, S.; Mallikarjun Sharada, S. Adsorbate-assisted migration of the

- metal atom in atomically dispersed catalysts: An ab initio molecular dynamics study. *The Journal of Chemical Physics* **2021**, *Accepted*.
- (45) Larsen, A. H.; Mortensen, J. J.; Blomqvist, J.; Castelli, I. E.; Christensen, R.; Dułak, M.; Friis, J.; Groves, M. N.; Hammer, B.; Hargus, C., et al. The atomic simulation environment—a Python library for working with atoms. *Journal of Physics: Condensed Matter* **2017**, *29*, 273002.
 - (46) Kresse, G.; Hafner, J. Ab initio molecular dynamics for liquid metals. *Physical Review B* **1993**, *47*, 558.
 - (47) Kresse, G.; Hafner, J. Ab initio molecular-dynamics simulation of the liquid-metal–amorphous-semiconductor transition in germanium. *Physical Review B* **1994**, *49*, 14251.
 - (48) Kresse, G.; Furthmüller, J. Efficiency of ab-initio total energy calculations for metals and semiconductors using a plane-wave basis set. *Computational Materials Science* **1996**, *6*, 15–50.
 - (49) Kresse, G.; Furthmüller, J. Efficient iterative schemes for ab initio total-energy calculations using a plane-wave basis set. *Physical Review B* **1996**, *54*, 11169.
 - (50) Sun, J.; Ruzsinszky, A.; Perdew, J. P. Strongly constrained and appropriately normed semilocal density functional. *Physical Review Letters* **2015**, *115*, 036402.
 - (51) Hinuma, Y.; Hayashi, H.; Kumagai, Y.; Tanaka, I.; Oba, F. Comparison of approximations in density functional theory calculations: Energetics and structure of binary oxides. *Physical Review B* **2017**, *96*, 094102.
 - (52) Zhang, Y.; Furness, J. W.; Xiao, B.; Sun, J. Subtlety of TiO₂ phase stability: Reliability of the density functional theory predictions and persistence of the self-interaction error. *The Journal of Chemical Physics* **2019**, *150*, 014105.

- (53) Yang, J. H.; Kitchaev, D. A.; Ceder, G. Rationalizing accurate structure prediction in the meta-GGA SCAN functional. *Physical Review B* **2019**, *100*, 035132.
- (54) Wang, Y.; Wen, B.; Dahal, A.; Kimmel, G. A.; Rousseau, R.; Selloni, A.; Petrik, N. G.; Dohnálek, Z. Binding of Formic Acid on Anatase TiO₂ (101). *The Journal of Physical Chemistry C* **2020**, *124*, 20228–20239.
- (55) Calegari Andrade, M. F.; Ko, H.-Y.; Car, R.; Selloni, A. Structure, polarization, and sum frequency generation spectrum of interfacial water on anatase TiO₂. *The Journal of Physical Chemistry Letters* **2018**, *9*, 6716–6721.
- (56) Campbell, C. T. Finding the Rate-Determining Step in a Mechanism: Comparing DeDonder Relations with the Degree of Rate Control. *Journal of Catalysis* **2001**, *204*, 520–524.
- (57) Liu, B.; Li, W.; Song, W.; Liu, J. Carbonate-mediated Mars–van Krevelen mechanism for CO oxidation on cobalt-doped ceria catalysts: facet-dependence and coordination-dependence. *Physical Chemistry Chemical Physics* **2018**, *20*, 16045–16059.
- (58) Sarma, B. B.; Plessow, P. N.; Agostini, G.; Concepción, P.; Pfander, N.; Kang, L.; Wang, F. R.; Studt, F.; Prieto, G. Metal-specific reactivity in single-atom catalysts: CO oxidation on 4d and 5d transition metals atomically dispersed on MgO. *Journal of the American Chemical Society* **2020**, *142*, 14890–14902.
- (59) Wang, F.; Wei, S.; Zhang, Z.; Patzke, G. R.; Zhou, Y. Oxygen vacancies as active sites for H₂S dissociation on the rutile TiO₂(110) surface: a first-principles study. *Physical Chemistry Chemical Physics* **2016**, *18*, 6706–6712.
- (60) Ammal, S. C.; Heyden, A. Water-gas shift activity of atomically dispersed cationic platinum versus metallic platinum clusters on titania supports. *ACS Catalysis* **2017**, *7*, 301–309.

- (61) Tang, Y.; Wang, Y.-G.; Li, J. Theoretical investigations of Pt1@ CeO2 single-atom catalyst for CO oxidation. *The Journal of Physical Chemistry C* **2017**, *121*, 11281–11289.
- (62) Peterson, E. J.; DeLaRiva, A. T.; Lin, S.; Johnson, R. S.; Guo, H.; Miller, J. T.; Kwak, J. H.; Peden, C. H.; Kiefer, B.; Allard, L. F., et al. Low-temperature carbon monoxide oxidation catalysed by regenerable atomically dispersed palladium on alumina. *Nature Communications* **2014**, *5*, 1–11.
- (63) Wang, X.; Ye, J.; Zhang, L.; Bu, Y.; Sun, W. Strain engineering to tune the performance of CO oxidation on Cu₂O (111) surface: A theoretical study. *Applied Surface Science* **2021**, *540*, 148331.
- (64) Lu, Y.-H.; Zhou, M.; Zhang, C.; Feng, Y.-P. Metal-embedded graphene: a possible catalyst with high activity. *The Journal of Physical Chemistry C* **2009**, *113*, 20156–20160.
- (65) Esrafil, M. D.; Asadollahi, S. A Single Pd Atom Stabilized on Boron-Vacancy of h-BN Nanosheet: A Promising Catalyst for CO Oxidation. *ChemistrySelect* **2018**, *3*, 9181–9188.
- (66) Ding, K.; Gulec, A.; Johnson, A. M.; Schweitzer, N. M.; Stucky, G. D.; Marks, L. D.; Stair, P. C. Identification of active sites in CO oxidation and water-gas shift over supported Pt catalysts. *Science* **2015**, *350*, 189–192.
- (67) Jakub, Z.; Hulva, J.; Meier, M.; Bliem, R.; Kraushofer, F.; Setvin, M.; Schmid, M.; Diebold, U.; Franchini, C.; Parkinson, G. S. Local Structure and Coordination Define Adsorption in a Model Ir₁/Fe₃O₄ Single-Atom Catalyst. *Angewandte Chemie* **2019**, *131*, 14099–14106.
- (68) Feng, X.; Liu, D.; Li, W.; Jin, X.; Zhang, Z.; Zhang, Y. Catalytic activity boost of

- CeO₂/Co₃O₄ nanospheres derived from CeCo-glycolate via yolk-shell structural evolution. *Inorganic Chemistry Frontiers* **2020**, *7*, 421–426.
- (69) Wang, Y.-G.; Cantu, D. C.; Lee, M.-S.; Li, J.; Glezakou, V.-A.; Rousseau, R. CO oxidation on Au/TiO₂: condition-dependent active sites and mechanistic pathways. *Journal of the American Chemical Society* **2016**, *138*, 10467–10476.
- (70) Jakub, Z.; Hulva, J.; Ryan, P. T.; Duncan, D. A.; Payne, D. J.; Bliem, R.; Ulreich, M.; Hofegger, P.; Kraushofer, F.; Meier, M., et al. Adsorbate-induced structural evolution changes the mechanism of CO oxidation on a Rh/Fe₃O₄ (001) model catalyst. *Nanoscale* **2020**, *12*, 5866–5875.
- (71) Nolan, M. Enhanced oxygen vacancy formation in ceria (111) and (110) surfaces doped with divalent cations. *Journal of Materials Chemistry* **2011**, *21*, 9160–9168.
- (72) Nolan, M.; Verdugo, V. S.; Metiu, H. Vacancy formation and CO adsorption on gold-doped ceria surfaces. *Surface Science* **2008**, *602*, 2734–2742.
- (73) Sakellson, S.; McMillan, M.; Haller, G. L. EXAFS evidence for direct metal-metal bonding in reduced rhodium/titania catalysts. *The Journal of Physical Chemistry* **1986**, *90*, 1733–1736.
- (74) Goodwin Jr, J. G.; Kim, S.; Rhodes, W. D. Turnover frequencies in metal catalysis: Meanings, functionalities and relationships. *Catalysis* **2007**, *17*, 320–347.